



Design, Characterization and Optimization of Multi-directional Bending Pneumatic Artificial Muscles

Wei Xiao^{1,2} · Dean Hu^{1,2} · Weixiong Chen^{1,2} · Gang Yang^{1,2} · Xu Han^{1,2,3}

Received: 31 January 2021 / Revised: 20 August 2021 / Accepted: 6 September 2021
© Jilin University 2021 2021

Abstract

Bending Pneumatic Artificial Muscles (PAMs) are particularly attractive and extensively applied to the soft grasper, snake-like robot, etc. To extend the application of PAMs, we fabricate a Multi-directional Bending Pneumatic Artificial Muscle (MBPAM) that can bend in eight directions by changing the pressurized chambers. The maximum bending angle and output force are 151° and 0.643 N under the pressure of 100 kPa, respectively. Additionally, the Finite Element Model (FEM) is established to further investigate the performance. The experimental and numerical results demonstrate the nonlinear relationship between the pressure and the bending angle and output force. Moreover, the effects of parameters on the performance are studied with the validated FEM. The results reveal that the amplitude of waves and the thickness of the base layer can be optimized. Thus, multi-objective optimization is performed to improve the bending performance of the MBPAM. The optimization results indicate that the output force can be increased by 7.8% with the identical bending angle of the initial design, while the bending angle can be improved by 8.6% with the same output force. Finally, the grasp tests demonstrate the grip capability of the soft four-finger gripper and display the application prospect of the MBPAM in soft robots.

Keywords Pneumatic artificial muscles · Multi-directional bending · Soft robots · Parameter optimization

1 Introduction

In recent years, widespread attention has been focused on the study of artificial muscles (soft actuators) owing to their great flexibility, easy fabrication, high environment adaptability, safety of human–robot interaction, and simple control. A variety of artificial muscles have been designed, such as shape memory alloy actuators [1, 2], electroactive polymer actuators [3, 4], liquid crystal polymers [5–7], and Pneumatic Artificial Muscles (PAMs) [8–11], which

results in many kinds of potential applications in the fields of soft robotics [8, 12, 13], medical devices [14, 15], wearable devices [16, 17], and flexible manipulators [18–20]. The most well-known and widely applied artificial muscles are the McKibben PAMs that can generate axial contraction and radial expansion [21, 22] when inflated by compressed fluids. To expand the application, various PAMs with specific structures are fabricated by soft material, which is able to bend [11, 19], rotate [12, 23], and twist [24, 25] upon pressurization.

The bending PAMs are hugely popular and always regarded as the subcategory of soft robots [26]. Their bending deformation is due to the asymmetric volumetric expansion of the soft chambers that are achieved by inflating the chambers nonuniformly or adding stiffness materials to the bending PAMs [27]. The PAMs bending in a single direction are well studied and have been widely applied in soft grippers and wearable gloves. For example, Hao et al. [28] designed a bending PAM using two silicone rubber with different stiffness, and the PAM was used to make a soft gripper. The fiber-reinforced bending PAM proposed by Polygerinos et al. [29] was a well-designed structure that provides a large bending angle, and the theoretical model was constructed to get a deep insight into the

✉ Dean Hu
hudean@hnu.edu.cn

¹ State Key Laboratory of Advanced Design and Manufacturing for Vehicle Body, College of Mechanical and Vehicle Engineering, Hunan University, Changsha 410082, People's Republic of China

² Key Laboratory of Advanced Design and Simulation Techniques for Special Equipment, Ministry of Education, Hunan University, Changsha 410082, People's Republic of China

³ School of Mechanical Engineering, Hebei University of Technology, Tianjin 300401, People's Republic of China

response of the PAM. The PAMs bending in one direction are not flexible enough, resulting in a limitation of their applications. Therefore, some bidirectional bending PAMs are developed, such as the soft actuators incorporating both positive and negative pressures [11] and the soft actuators with two separate chambers [30, 31]. These PAMs are capable of extending the grasping ability of soft grippers and enhancing the mobility of movements for soft robots. However, the bidirectional bending PAMs can only work in a two-dimensional plane, which is not sufficient for executing complicated tasks and adapting to unstructured environments [32].

In practical applications, the soft grippers fabricated with bending PAMs are expected to grasp objects with different shapes and sizes, and the soft robots also need to adjust the heading direction in three-dimensional space. As a result, researchers aim to design bending PAMs with multi-direction [20, 32–34] to tackle the challenges. The study of the multi-directional bending PAMs is relatively fewer compared with that of the PAMs bending in one direction or two directions. In addition, most of the existing multi-directional bending PAMs are realized by the fiber-reinforced structures with different shaped chambers [20, 32, 33]. Theoretically, these fiber-reinforced PAMs can bend in arbitrary directions by controlling the pressure applied to the chambers. In fact, the constant pressure is generally applied to one chamber or two chambers to simplify the control system [35]. On the other hand, the winding fiber around the elastomer increases the complexity of fabrication, and the manual winding also leads to an uneven distribution of the fibers. Hence, it is significant that the multi-directional bending PAMs can be fabricated easily and possess a bigger working area.

In this paper, we present a multi-directional bending PAM with four cosine shape chambers, which can bend in eight directions by pressurizing the chambers with the same pressure. This PAM can be fabricated easily with three simple steps by the improvement of the typical fabrication method. Experiment tests and finite element analysis are carried out to investigate their bending performance. On the basis of the validated finite element model, the metamodel of the PAM is constructed. Then the multi-objective optimization is performed based on the metamodel method to seek the optimal parameters of the PAM. Finally, a soft four-finger gripper is designed with the proposed multi-directional bending PAM, and the grasp tests demonstrate the application prospect of the PAM.

2 Actuator Samples and Research Methods

2.1 Design and Fabrication of the MBPAM

The multi-directional bending pneumatic artificial muscle (MBPAM) is shown in Fig. 1, previously proposed in our

earlier work [36]. The MBPAM possesses a slender structure with a length of 130 mm and a radius of 10 mm. At the end of the MBPAM, there are four pneumatic tubes that connect four separate air chambers, respectively. In the initial design, the length and thickness of cosine shape chambers are 105 mm and 2 mm, respectively. Each chamber has 14 waves with an amplitude (a) of 2.5 mm. The cross-shaped base layer with a thickness (b) of 2 mm is mainly used for isolating the chambers and restricting the axial elongation and the radial expansion of the MBPAM. The MBPAM provides two working patterns, namely pressurizing a single chamber (PSC) and pressurizing double adjacent chambers (PDC). Thus, it has eight basic deflections when highly compressed fluids are applied to one chamber or two chambers.

To fabricate the MBPAM, we use the casting method that has been successfully applied to fabricate the PAM with a simple structure [32]. In the typical fabrication process, the cured silicone rubber is completely unmolded from molds [18, 20, 36], which may lead to the difficulties in fixing the position of the cured silicone rubber and controlling the thickness of the layer used for sealing chambers. Herein, the casting method with some improvements is employed to manufacture the MBPAM. As displayed in Fig. 2, the cured silicone rubber stays in mold A until the process is completed, which can overcome the difficulties in the typical fabrication step. Before actuator casting, all of the molds were fabricated by a commercial 3D printer which can provide an acceptable fabrication accuracy of ± 0.1 mm. The accuracy of the molds will directly affect the precision of the MBPAM. To further ensure the accuracy of the molding, two sets of molds were made and examined, and the more accurate molds were used in the actuator casting. First, two components of liquid silicone (E625) were mixed at a 1:1 weight ratio. The mixture was settled in a vacuum for 3 min – 5 min to let the air bubbles rise out, and then the mixture was poured into the assembled mold. Three hours

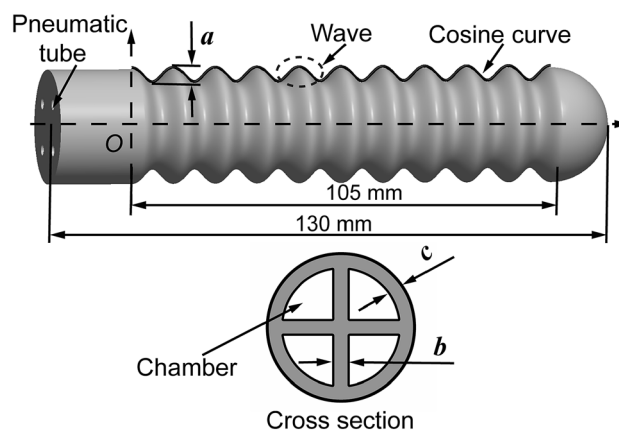
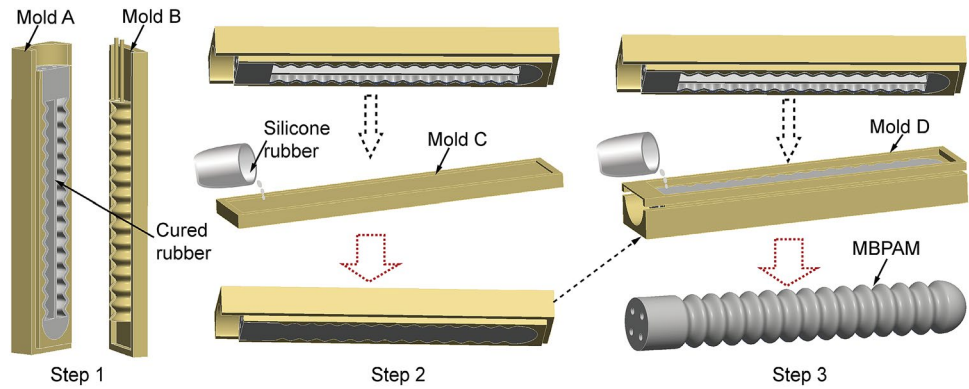


Fig. 1 Structural diagram of the MBPAM

Fig. 2 Fabrication process of the MBPAM. Step1: fabricating the half of MBPAM with two open chambers. Step2: sealing the half of MBPAM with uncured silicone rubber. Step3: cementing the half of the unsealed MBPAM and the half of the sealed MBPAM together via uncured silicone rubber



later, the mold B can be removed while the cured silicone rubber was still left in mold A (Step 1 of Fig. 2). Second, the half of MBPAM with two open chambers was sealed by applying a thin layer of the silicone rubber (1 mm) on the mold C (Step 2 of Fig. 2). Finally, the mold D was mounted above the half of the sealed MBPAM that still stays in mold A. We were cemented the half of unsealed MBPAM and the half of sealed MBPAM together via uncured silicone rubber (Step 3 of Fig. 2).

2.2 Testing of the MBPAM

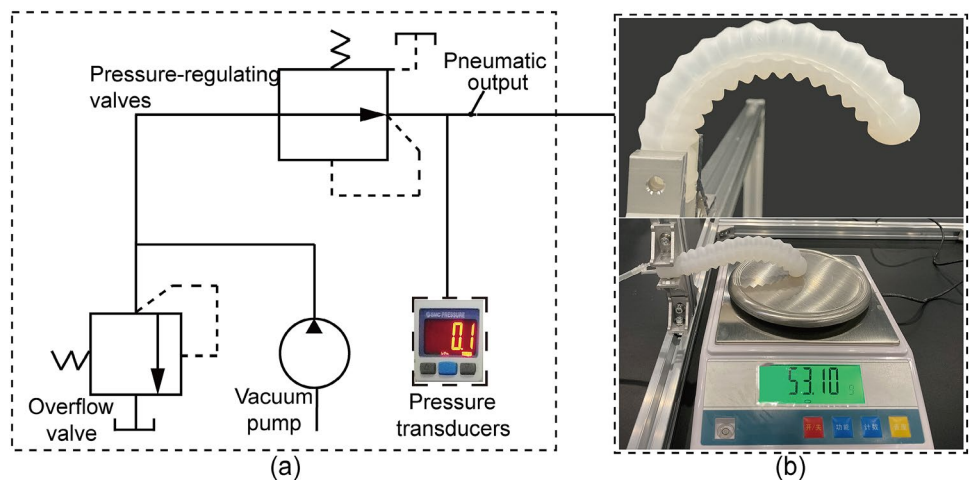
To characterize the bending ability of the MBPAM, a measurement system was constructed as shown in Fig. 3. The device of the generation of compressed fluids contains an air pump, an overflow valve, a pressure-regulating valve, and a pressure transducer, which can provide steady and pressure adjustable fluids for actuating the MBPAM. When the MBPAM was actuated by specific pressure, the deformation of MBPAM was recorded with a camera (Fig. 3b). The post-process was carried out by employing the graphics processing software to obtain the bending angle. The output force of the MBPAM could be obtained by utilizing the test setup displayed in Fig. 3b. The force exerted by the MBPAM

was measured with a digital scale as the end of the actuator was mounted on the platform. Note that the digital scale was zeroed before actuating the MBPAM and the output force should be recorded after the pressure holding for a while to obtain the steady-state situation of the MBPAM.

2.3 Finite Element Modeling

The finite element method as an effective way is widely used in investigating the response of flexible structures and non-linear materials. Therefore, this paper uses the finite element software ABAQUS/standard to further study the bending ability of the MBPAM. In general, Mooney-Rivlin [37], Ogden [38] and Yeoh [39] models are generic hyperelastic models, which are suitable for simulating silicone rubber. Mooney-Rivlin model is commonly used to describe the rubber with small or medium deformation. Ogden and Yeoh models are both appropriate for modeling the rubber with large deformation, while the Yeoh model possesses fewer material parameters than the Ogden model. Thus, the Yeoh material model is employed to simulate the behavior of the hyperelastic material in the finite element model (FEM), and its strain energy function can be written as follows [39]:

Fig. 3 Measurement system of the bending ability of the MBPAM. **a** Device of the generation of compressed fluids. **b** Measurement of the bending angle and output force of the MBPAM



$$U = \sum_{i=1}^3 C_{i0} (I_1 - 3)^i \quad (1)$$

where I_1 is the first deviatoric strain invariant, and C_{i0} is the material coefficient. To obtain the material coefficients, uniaxial tensile tests were carried out based on the standard ISO 37. Then the experimental data of uniaxial tensile were imported into ABAQUS to fit the material coefficients (Fig. 4a). Finally, we can obtain the material coefficients of the silicone rubber: $C_{10}=0.1154$ MPa, $C_{20}=-0.0091$ MPa, $C_{30}=0.0055$ MPa.

To model the bending behavior of the MBPAM, the 3D model without inlet was imported into ABAQUS and meshed with the solid tetrahedral linear hybrid elements. A uniformly distributed pressure was applied to the internal walls of chambers. The gravity of the MBPAM was also considered. In the FEM, the bottom of the MBPAM was fixed completely while the top of the MBPAM was free (Fig. 4b). The bending deformation of the MBPAM can be obtained as pressures are acted on the chambers, as depicted in Fig. 4b. When external obstacles existed the deformation of the free end was constrained, resulting in an output force in the free end of the MBPAM. To obtain the output force, a fixed plate was placed in the free end of the MBPAM. The linear elastic model was used to simulate the material behavior of the plate with the Elastic Modulus of 210 GPa and the Poisson ratio of 0.28. The tangential contact behavior between the plate and the MBPAM was simulated using the penalty method with a friction coefficient of 0.6. The normal contact behavior was viewed as ‘hard’ contact allowing separate after contact. In this way, the contact force between the obstacle and the MBPAM can be calculated at the bottom of the plate, which was equal to the output force of the MBPAM.

3 Performance Study

3.1 Characterization of the MBPAM

Based on numerical and experimental methods, we are capable of investigating the bending ability of the MBPAM effectively and conveniently. The bending angle and output force are demonstrated in Fig. 5 as one chamber and double chambers of MBPAM are subjected to positive pressure, respectively. The influence of mesh quantity on the response of the MBPAM is studied first. Numerical results with different mesh quantities are in essential agreement, which demonstrates that the results are mesh-independent. During the experiment, we have prepared two samples and each sample is tested twice. The experimental results plotted in Fig. 5 are averages of the four tests. The match of numerical and experimental results is excellent on the whole, with some deviation at part of the pressure levels due to the highly non-linear response exhibited by the MBPAM. Therefore, this agreement indicates the validity of the FEM in predicting the bending angle and output force of the MBPAM. Figure 5 also shows that the bending angle of the MBPAM increases nonlinearly with the pressure applied to the chambers. When the pressure of 100 kPa is applied to the MBPAM, the bending angles for the working patterns of PSC and PDC are 120° and 151° , respectively. For the output force, it has the same changing tendency as the bending angle. Experimental results show that the maximum output forces for PSC and PDC are 0.466 N and 0.643 N, respectively.

3.2 Effect of Structure Parameters

When the overall size (length: 130 mm, radius: 10 mm) of the MBPAM is fixed, there are four main parameters that affect their performance, including the amplitude of waves (a), the thickness of the cross-shaped base layer (b), the thickness of the chamber (c), and the number of waves

Fig. 4 Finite element analysis of the MBPAM. **a** Stress–strain curves for the silicone rubber based on the experimental data and Yeoh model data. **b** Eight basic deflections when different chambers are subject to pressure

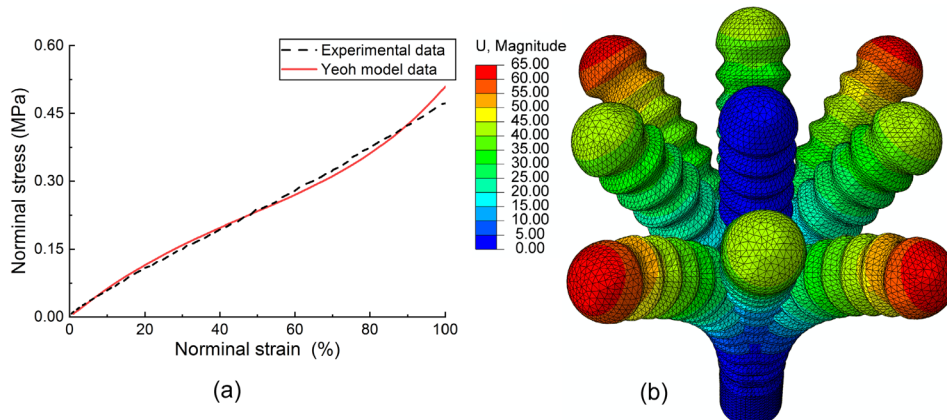
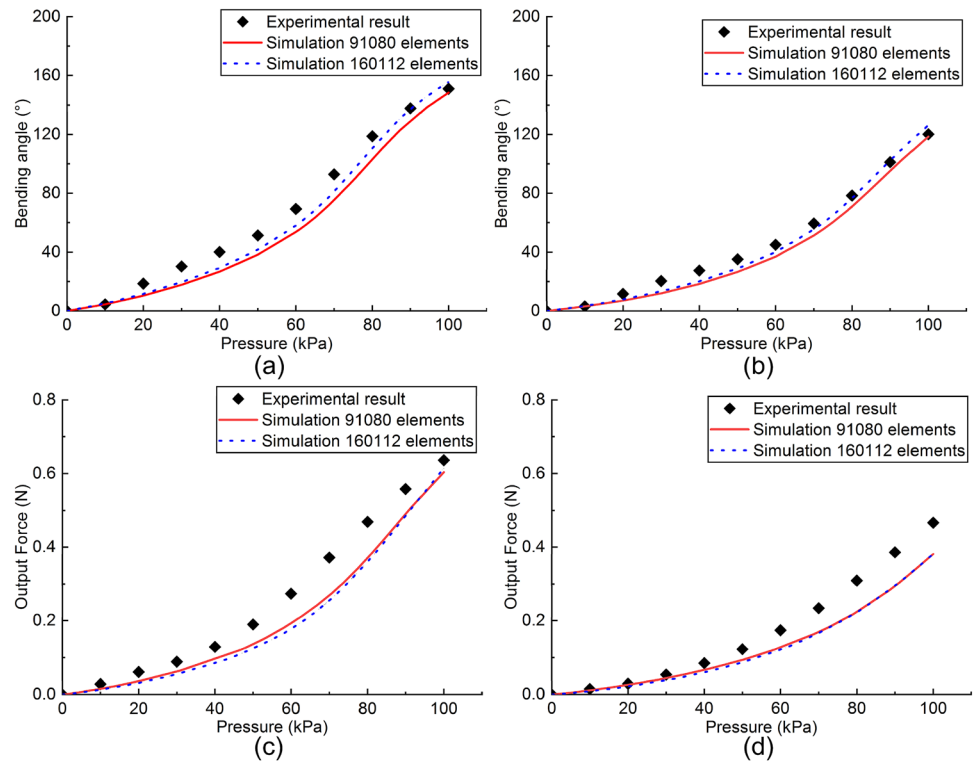


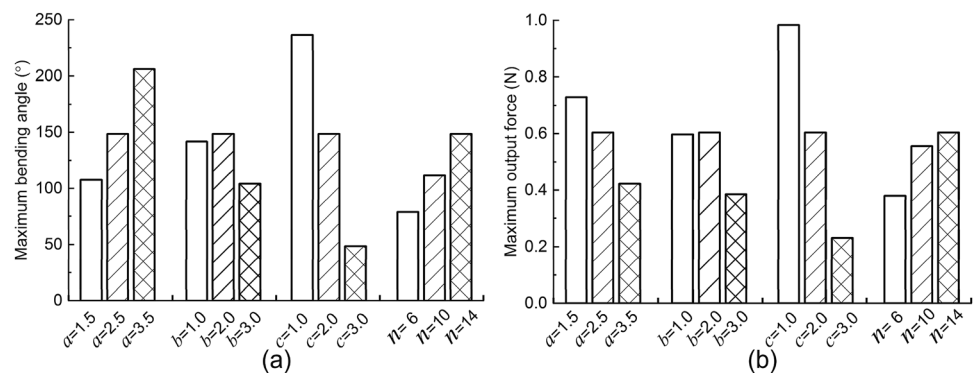
Fig. 5 Bending performance of the MBPAM when different pressures is applied to the chambers. **a** Bending angle for the working patterns of PDC. **b** Bending angle the working patterns of PSC. **c** Output force the working patterns of PDC. **d** Output force the working patterns of PSC



(*n*). Herein, the effects of the parameters on the response of the MBPAM are studied with the validated FEM. Since the bending performance of the MBPAM for the working patterns of PSC and PDC possesses an identical varying tendency with respect to the applied pressure, the working pattern of PDC is considered during the simulation. Three levels are selected for each of the parameters. The other three parameters remain unchanged when one of the parameters changes. The ranges of each parameter discussed in this paper are chosen as follows: $1.5 \text{ mm} \leq a \leq 3.5 \text{ mm}$, $1.0 \text{ mm} \leq b \leq 3.0 \text{ mm}$, $1.0 \text{ mm} \leq c \leq 3.0 \text{ mm}$, and $6 \leq n \leq 14$. The final bending angle and output force are extracted from the FEM in which the pressure of 100 kPa is applied to the chambers. The numerical results are illustrated in Fig. 6. As the amplitude of waves (*a*) is increased from 1.5 mm

to 3.5 mm, the maximum bending angle of the MBPAM rises whereas the maximum output force decreases, which exhibits a conflicting relationship between the design goals of the maximum bending angle and maximum output force. According to Fig. 6, the maximum bending angle and output force increase and then decrease with the growth of the thickness of the cross-shaped base layer (*b*). Thus, there is an optimal thickness of the cross-shaped base layer for the MBPAM. Both the maximum bending angle and output force decrease with the rising thickness of the chamber (*c*). Theoretically, the smaller the thickness of the chamber, the better the performance of the MBPAM. On the other hand, the decrease in the thickness of chambers will increase the possibility of the chamber explosion. Consequently, the appropriate thickness of the chamber is of great importance

Fig. 6 Effect of the parameters on the performance of the MBPAM. **a** Maximum bending angle of the actuator with different parameter configurations. **b** Maximum output force of the actuator with different parameter configurations



to balance the performance and reliability of the MBPAM. As for the number of waves (n), its growth can effectively improve the bending ability of the actuator. Though the four parameters are discretized in a limited range, the influence of the parameters on the bending ability of the MBPAM is revealed in general, which contributes to the following research of parameter optimization.

4 Multi-objective Optimization

In real applications, artificial muscles are always expected to bend in a larger range and to possess an acceptable output force. Based on the above study, we know that the bending angle and output force can be greatly influenced by the parameters of the MBPAM. However, it is difficult to know what the optimal parameters of the MBPAM would be. Herein, we are committed to seeking the optimal parameters to improve the performance of the MBPAM. In this study, we employ the method of multi-objective optimization design (MOD) to determine the optimal parameters of the MBPAM, and the flowchart of the implementation of parameter optimization is illustrated in Fig. 7.

4.1 Design of Experiment (DOE)

There are four parameters affecting the bending ability of the MBPAM. Since the bending angle and output force increase or decrease monotonously with the increase of the number

of waves (n) and thickness of the chamber (c), the amplitude of waves (a) and thickness of the cross-shaped base layer (b) are only considered in the parameter optimization problem. The maximum bending angle (θ_{\max}) and output force (F_{\max}) are chosen as objective functions when the pressure of 100 kPa is applied to the MBPAM. The Optimal Latin Hypercube Design (OLHD) [40] is used for the selection of sample points in the design space. By implementing the OLHD, twenty-one sample points are selected for the finite element analysis. The sample points and corresponding numerical results are summarized in Table 1.

4.2 Metamodel Establishment and Error Metrics

The metamodel provides an effective method to get accurate mathematical formulations of the relationship between the input and the response. Furthermore, it can significantly reduce the computational cost of finite element analysis. Thus, the metamodels are extensively employed in the optimization problem. In this paper, three different metamodels of Polynomial Response Surface (PRS) [41], Radial Basis Function (RBF) [42], and Kriging (KRG) [43] are established individually.

PRS as a widely used metamodel has been demonstrated to be suitable for approximation problems with nonlinearity [44]. In this method, the true value of experiments $y(\mathbf{x})$ at the point \mathbf{x} in the design space is modeled by [41]:

Table 1 Sample points and corresponding numerical results

No	a (mm)	b (mm)	θ_{\max} (°)	F_{\max} (N)
1	3.5	2.5	176.3913	0.3152
2	2.2	1.8	140.6596	0.6642
3	2.1	3.0	96.9420	0.4295
4	2.5	2.2	141.7004	0.5281
5	3.0	2.4	148.3988	0.3861
6	1.7	1.7	124.0175	0.7360
7	2.8	1.9	161.2707	0.5215
8	2.9	1.2	173.1479	0.5978
9	1.5	2.1	102.6996	0.6588
10	3.3	2.0	184.4651	0.4117
11	2.3	2.6	118.8059	0.4818
12	3.2	2.9	125.1550	0.2816
13	1.6	2.7	98.9534	0.5885
14	1.8	1.0	111.3608	0.6311
15	2.0	1.4	132.2590	0.6854
16	3.1	1.6	182.9210	0.5242
17	2.7	2.8	117.3126	0.3633
18	2.6	1.5	160.3739	0.6321
19	1.9	2.3	119.8800	0.6382
20	2.4	1.1	134.3892	0.6150
21	3.4	1.3	207.9520	0.5358

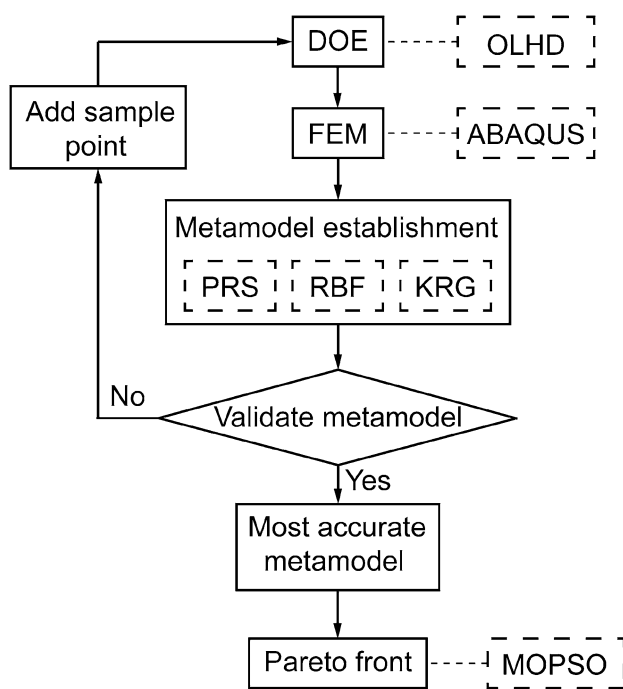


Fig. 7 Flowchart of the implementation of the parameter optimization

$$y(\mathbf{x}) = \varepsilon + \sum_{i=1}^n b_i f_i(\mathbf{x}) \quad (2)$$

where ε is the error between approximate values and actual values, i is the number of basis functions $f_i(\mathbf{x})$, b_i is the coefficient of the basis function. The approximate value $\tilde{y}(\mathbf{x})$ of the design objectives can be obtained from the following equation:

$$\tilde{y}(\mathbf{x}) = \sum_{i=1}^n \beta_i f_i(\mathbf{x}) \quad (3)$$

where the β_i is the estimator of the coefficient b_i . The coefficient β_i can be derived with the least-squares method based on the response surface theory. Herein, the cubic polynomial function without high-order cross terms is used to establish the PRS model.

RBF is capable of establishing a reasonably accurate metamodel with fewer sample points, and its mathematical form can be written as [42]

$$\tilde{y}(\mathbf{x}) = \sum_{i=1}^m \lambda_i \rho(\mathbf{x}, \mathbf{x}_i) \quad (4)$$

where m is the number of neurons, λ_i the weights of the linear combination of neurons, $\rho(\mathbf{x}, \mathbf{x}_i)$ is the radial basis function. Gaussian basic function is chosen in the RBF metamodels. And the coefficients of the RBF metamodels can be obtained based on the response values of the sample points.

KRG has been frequently used in the optimization design due to the high approximation accuracy for many nonlinear problems. Equation (5) shows the mathematical form of KRG that combines the known function (such as the polynomial function) and the departures [43].

$$\tilde{y}(\mathbf{x}) = \sum_{i=1}^k \varphi_i h_i(\mathbf{x}) + z(\mathbf{x}) \quad (5)$$

where $z(\mathbf{x})$ is the departure of the model. The corresponding coefficients of the KRG metamodels can be calculated based on the kriging principle.

To choose the most accurate metamodel, three error estimators, including the maximum relative error (MRE), coefficient of determination (R^2), and root mean square error ($RMSE$), are used to assess the accuracy of the metamodels. R^2 and $RMSE$ are the overall accuracies of the metamodels, whereas MRE represents the local precision. The values of MRE , R^2 , and $RMSE$ can be calculated with the following equations:

$$MRE = \text{Max} \left(\frac{|y_i - \tilde{y}_i|}{y_i} \right) \quad (6)$$

$$R^2 = 1 - \frac{\sum_{i=1}^u (y_i - \tilde{y}_i)^2}{\sum_{i=1}^u (y_i - \bar{y})^2} \quad (7)$$

$$RMSE = \sqrt{\frac{\sum_{i=1}^u (y_i - \tilde{y}_i)^2}{u}} \quad (8)$$

where u represents the number of the validation samples, y_i and \tilde{y}_i are the numerical data and the corresponding data estimated by the metamodels, respectively, \bar{y} denotes the mean of y_i . To evaluate the accuracy of the metamodels, additional 8 sample points are chosen and the corresponding numerical results are listed in Table 2. The accuracy evaluation for different metamodels is demonstrated in Table 3. Generally, the closer value to zero of MRE and $RMSE$, and the larger value of R^2 , demonstrate the higher accuracy of the metamodels. Hence, the PRS metamodels possess the highest precision than the RBF and KRG metamodels. The objective functions θ_{\max} and F_{\max} of the PRS metamodels are expressed as follows:

$$\begin{aligned} \theta_{\max} = & -329.2005 + 339.6515a + 203.7575b - 118.5423a^2 \\ & - 69.3005b^2 - 17.2730ab + 16.9488a^3 + 7.4029b^3 \end{aligned} \quad (9)$$

$$\begin{aligned} F_{\max} = & -0.6614 + 0.8489a + 1.2680b - 0.3633a^2 - 0.5750b^2 \\ & - 0.0491ab + 0.0475a^3 + 0.0809b^3 \end{aligned} \quad (10)$$

Based on the above expressions, the θ_{\max} and F_{\max} with respect to the design variables a and b are plotted in Fig. 8, which illustrates the relationship between the objective function and the design variables visually.

4.3 Multi-objective Optimization

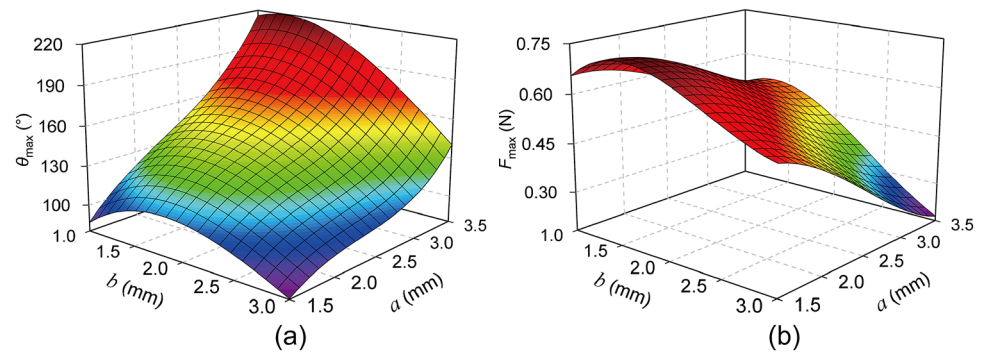
The multi-objective optimization aims at maximizing the bending angle and the output force of the MBPAM. The

Table 2 Validation samples and corresponding numerical results

No	a (mm)	b (mm)	θ_{\max} (°)	F_{\max} (N)
1	2.5	2.0	148.4230	0.6036
2	1.9	2.7	106.7603	0.5382
3	3.5	2.0	206.2165	0.4226
4	2.5	1.0	141.7800	0.5964
5	3.0	2.7	130.6031	0.3359
6	2.5	3.0	104.1660	0.3850
7	1.5	2.0	107.6123	0.7294
8	2.0	1.8	132.1826	0.6893

Table 3 Accuracy evaluation of the metamodels

Metamodel	θ_{\max}			F_{\max}		
	R^2	$RMSE$	MRE	R^2	$RMSE$	MRE
PRS	0.9964	0.0184	0.0340	0.9776	0.0511	0.0982
RBF	0.9879	0.0337	0.0849	0.9607	0.0678	0.1333
KRG	0.9831	0.0399	0.0826	0.9618	0.0669	0.1345

Fig. 8 PRS metamodels of different objectives of the MBPAM: **a** Maximum bending angle (θ_{\max}). **b** Maximum output force (F_{\max})**Table 4** Details of parameter settings used in the MOPSO

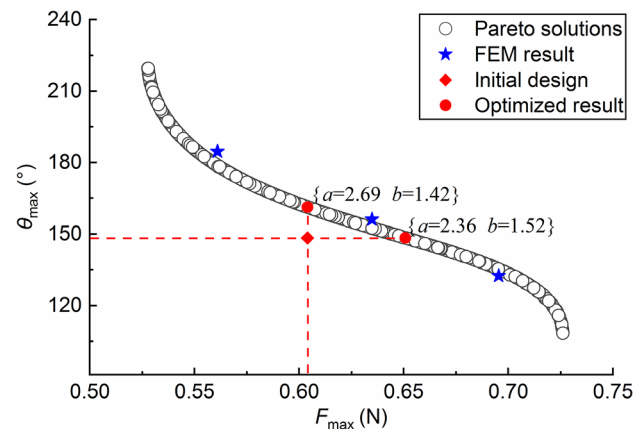
MOPSO parameters	Value
Maximum iterations	100
Number of particles	100
Inertia	0.8
Global increment	0.5
Particle increment	0.9
Maximum velocity	0.1
Max failed runs	5

multi-objective optimization problem can be defined mathematically as

$$\begin{cases} \text{Min} [-\theta_{\max}(a, b), -F_{\max}(a, b)] \\ \text{s.t. } 1.5 \leq a \leq 3.5 \\ 1.0 \leq b \leq 3.0 \end{cases} \quad (11)$$

The multi-objective particle swarm optimization (MOPSO), characterized by a rapid convergence and well-distributed Pareto solutions [44, 45], is used on the most accurate metamodels of PRS to obtain Pareto solutions in this study. The details of the parameter settings used in the MOPSO are listed in Table 4.

The optimization results are determined after running the MOPSO algorithm, and the Pareto solutions are depicted in Fig. 9. To validate the Pareto solutions, three optimal designs were selected and simulated with the finite element method. The numerical results for the optimal designs are plotted in Fig. 9. The metamodel-based optimization results match very well with the FEM results, and the maximum errors of θ_{\max} and F_{\max} predicted by the PRS models are less

**Fig. 9** Pareto solutions of the MBPAM and numerical results of the three optimal designs

than 2% (Table 5). This demonstrates that the optimization results from MOD are reasonable and reliable. According to Fig. 9, we observe that the design objectives cannot achieve the optimum concurrently. Hence, a compromise solution satisfying the performance requirement needs to be determined on the basis of the Pareto solutions. Additionally, we can find that the initial design is under the Pareto solutions, which means that the parameters of the initial design can be optimized further. Compared with the initial design, the output force can be improved by 7.8% when the bending angle is the same, while the bending angle can be increased by 8.6% with the identical output force. This indicates that the multi-objective optimization design plays a significant role in the design of the MBPAM.

In summary, the metamodel-based optimization method as a significant approach in mechanical design is

Table 5 Validation of the PRS metamodel-based optimization results

No	a (mm)	b (mm)	θ_{\max}			F_{\max}		
			PRS	FEM	Error (%)	PRS	FEM	Error (%)
1	3.12	1.36	185.27	184.49	0.42	0.5504	0.5611	1.91
2	2.54	1.42	155.20	156.01	0.52	0.6251	0.6350	1.56
3	1.98	1.46	133.12	132.32	0.60	0.7007	0.6955	0.75

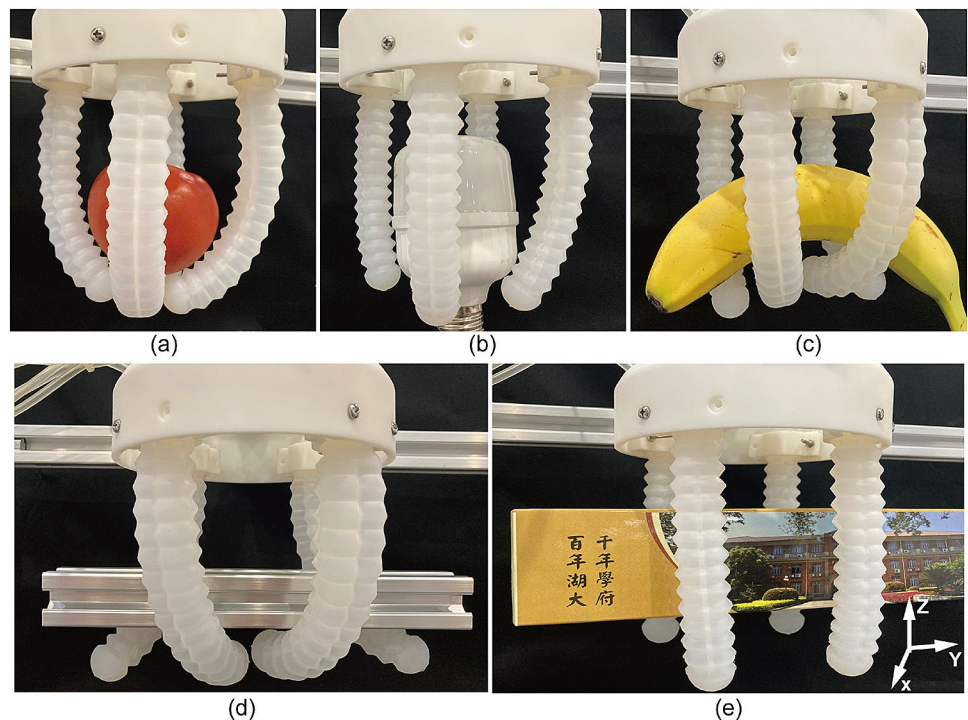
successfully applied to the design of the MBPAM. Furthermore, the metamodel-based optimization method can be also employed to the design of multi-directional PAMs with different sizes and general versatility. The key to the implementation of parameter optimization is that the metamodel needs to be constructed accurately based on the structure of PAMs.

5 Application: Soft Gripper

A soft four-finger gripper was designed to demonstrate the potential application of the MBPAM, as shown in Fig. 10. The housing was fabricated with a commercial 3D printer, which can hold four MBPAMs that are equidistant from one another. The MBPAM was mounted on the housing using bolts. The developed four-finger gripper is able to grasp a variety of objects, such as the tomato, bulb, banana, aluminum tube, and carton. These objects have different sizes and shapes, which are selected carefully to be representative. As shown in Fig. 10a and b, the four MBPAMs bend inward simultaneously to grasp the tomato and bulb. The

gripper is also employed to grasp rod-like objects, including the banana, aluminum tube, and carton. Figure 10 exhibits three grasp modes by controlling the inflating chambers of the MBPAMs. For the first grasp mode, two of the MBPAMs bend in the XZ plane (XZ plane is perpendicular to objects) and the others bend in the plane that has an angle of -45° to the XZ plane, as illustrated in Fig. 10c. The first grasp mode is suitable for gripping rod-like objects with a relatively shorter length. The second grasp mode is effective in grasping the slender objects, as displayed in Fig. 10d. The MBPAMs bend in the plane rotated -45° around the Z -axis. As for the third grasp mode, all of the MBPAMs bend in the XZ plane, which is applicable for the grip of mid-length objects. Different grasp modes can be achieved by controlling the inflating chambers. Figure 11 demonstrates the control strategy for grasping various objects. To control the gripper easily and effectively, the chambers of the soft gripper are numbered firstly. Different grasp modes are corresponding to the specific combination of inflating chambers, as shown in Fig. 11. The objects with different sizes and shapes can be detected by a camera, which is employed

Fig. 10 Grasping experiments with a four-finger gripper. **a** Tomato: 183 g. **b** Bulb: 46 g. **c** Banana: 180 g. **d** Aluminum tube: 118 g. **e** Carton: 48 g



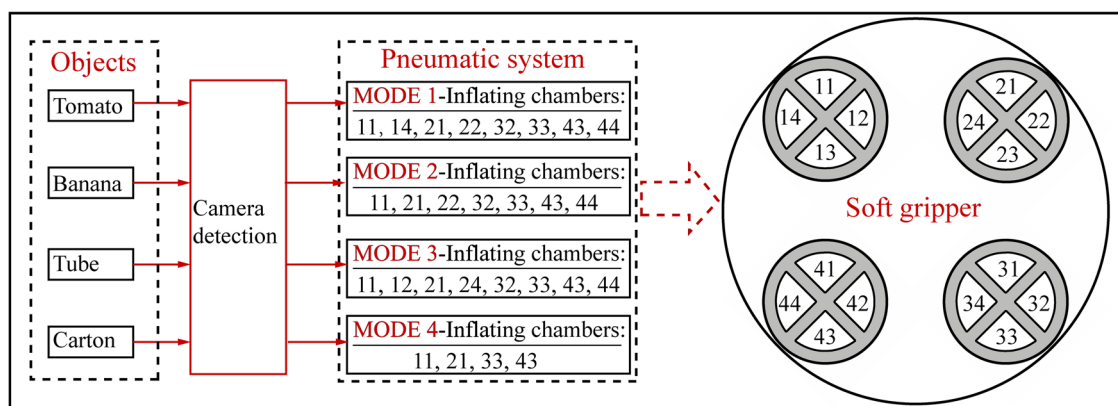


Fig. 11 Control strategy of different grasp modes for grasping various objects

to decide the grasp modes. At the current stage, the decision of the grasp modes is made artificially in the experiments to demonstrate the capability of the soft gripper. In our future work, an intelligent control system needs to be implemented for broadening the application of the soft gripper.

In brief, these grasp modes greatly extend the capability of this gripper, which is not available in the existing soft grippers [46]. In addition, the grasp tests demonstrate the novelty and capability of the soft four-finger gripper and the broad application prospect of the MBPAM.

6 Conclusion

In conclusion, in this study, we fabricate a multi-directional bending pneumatic artificial muscle that possesses two working patterns of PSC and PDC. The experimental results show that the bending angle and output force present the nonlinear growth tendency along with the increase of the pressure applied to chambers. When the MBPAM is subjected to the uniform pressure of 100 kPa, the bending angle for PSC and PDC are 120° and 151° , and the output force for PSC and PDC are 0.466 N and 0.643 N. The finite element model is also developed to investigate the bending performance of the MBPAM, and experimental tests are carried out to validate the FEM. The excellent agreement between the numerical and experimental results indicates the validity of the FEM. Based on the validated FEM and the constructed metamodel, the multi-objective optimization design is carried out to optimize the parameters of the MBPAM. The Pareto solutions are obtained after performing the MOD, which indicates that the bending angle and output force cannot achieve the optimum concurrently and a compromise solution needs to be selected. And the bending angle and output force of the initial design also can be improved according to the Pareto solutions. Additionally, the soft four-finger gripper is fabricated by using a housing and

four MBPAMs. The gripper is capable of grasping a broad range of objects owing to the multiple bending directions of the MBPAM. Therefore, the proposed MBPAM exhibits attractive prospects in the soft machines, such as the universal gripper of the pickup of fruits, vegetables, etc.

Acknowledgements The supports from the National Natural Science Foundation of China (11872178, 51621004) are gratefully acknowledged.

Declarations

Conflict of interest The authors declare no conflict of interest.

References

1. Laschi, C., Cianchetti, M., Mazzolai, B., Margheri, L., Follador, M., & Dario, P. (2012). Soft robot arm inspired by the octopus. *Advanced Robotics*, 26, 709–727.
2. She, Y., Li, C., Cleary, J., & Su, H. (2015). Design and fabrication of a soft robotic hand with embedded actuators and sensors. *Journal of Mechanisms and Robotics*, 7, 21007.
3. Hajiesmaili, E., & Clarke, D. R. (2019). Reconfigurable shape-morphing dielectric elastomers using spatially varying electric fields. *Nature Communications*, 10, 1–7.
4. Cianchetti, M., Mattoli, V., Mazzolai, B., Laschi, C., & Dario, P. (2009). A new design methodology of electrostrictive actuators for bio-inspired robotics. *Sensors and Actuators B: Chemical*, 142, 288–297.
5. Xiao, Y. Y., Jiang, Z. C., Tong, X., & Zhao, Y. (2019). Biomimetic locomotion of electrically powered “janus” soft robots using a liquid crystal polymer. *Advanced Materials*, 31, 1903452.
6. Shahsavan, H., Salili, S. M., Jákli, A., & Zhao, B. (2017). Thermally active liquid crystal network gripper mimicking the self-peeling of gecko toe pads. *Advanced Materials*, 29, 1604021.
7. He, Q. G., Wang, Z. J., Song, Z. Q., & Cai, S. Q. (2019). Bioinspired design of vascular artificial muscle. *Advanced Materials Technologies*, 4, 1800244.
8. Kim, W., Byun, J., Kim, J., Choi, W., Jakobsen, K., Jakobsen, J., Lee, D., & Cho, K. (2019). Bioinspired dual-morphing stretchable origami. *Science Robotics*, 4, y3493.

9. Wang, Z., & Hirai, S. (2017). Soft gripper dynamics using a line-segment model with an optimization-based parameter identification method. *Ieee Robotics and Automation Letters*, 2, 624–631.
10. Chen, Y. X., Hu, B. B., Zou, J. K., Zhang, W., Wang, D. S., & Jin, G. Q. (2020). Design and fabrication of a multi-motion mode soft crawling robot. *Journal of Bionic Engineering*, 17, 932–943.
11. Hao, Y., Gong, Z. Y., Xie, Z. X., Guan, S. Y., Yang, X. B., Wang, T. M., & Wen, L. (2018). A soft bionic gripper with variable effective length. *Journal of Bionic Engineering*, 15, 220–235.
12. Ainla, A., Verma, M. S., Yang, D., & Whitesides, G. M. (2017). Soft, rotating pneumatic actuator. *Soft Robotics*, 4, 297–304.
13. Gu, G., Zou, J., Zhao, R., Zhao, X., & Zhu, X. (2018). Soft wall-climbing robots. *Science. Robotics*, 3, t2874.
14. De Falco, I., Cianchetti, M., & Menciassi, A. (2017). A soft multi-module manipulator with variable stiffness for minimally invasive surgery. *Bioinspiration & Biomimetics*, 12, 56008.
15. Yan, J., Zhang, X., Xu, B., & Zhao, J. (2018). A new spiral-type inflatable pure torsional soft actuator. *Soft Robotics*, 5, 527–540.
16. Yeo, J. C., Yap, H. K., Xi, W., Wang, Z., Yeow, C. H., & Lim, C. T. (2016). Flexible and stretchable strain sensing actuator for wearable soft robotic applications. *Advanced Materials Technologies*, 1, 1600018.
17. Koo, I. M., Jung, K., Koo, J. C., Nam, J., Lee, Y. K., & Choi, H. R. (2008). Development of soft-actuator-based wearable tactile display. *Ieee Transactions on Robotics*, 24, 549–558.
18. Xiao, W., Hu, D., Chen, W. X., Yang, G., & Han, X. (2021). A new type of soft pneumatic torsional actuator with helical chambers for flexible machines. *Journal of Mechanisms and Robotics*, 13, 11003.
19. Alici, G., Canty, T., Mutlu, R., Hu, W., & Sencadas, V. (2018). Modeling and experimental evaluation of bending behavior of soft pneumatic actuators made of discrete actuation chambers. *Soft Robotics*, 5, 24–35.
20. Gong, Z. Y., Fang, X., Chen, X. Y., Cheng, J. H., Xie, Z. X., Liu, J. Q., Chen, B. H., Yang, H., Kong, S. H., Hao, Y. F., Wang, T. M., Yu, J. Z., & Wen, L. (2021). A soft manipulator for efficient delicate grasping in shallow water: modeling, control, and real-world experiments. *The International Journal of Robotics Research*, 40, 449–469.
21. Chou, C., & Hannaford, B. (1996). Measurement and modeling of mckibben pneumatic artificial muscles. *IEEE Transactions on robotics and automation*, 12, 90–102.
22. Schulte, H. (1961). The application of external power in prosthetics and orthotics. *The Characteristics of the McKibben Artificial Muscle*, National Research Council, 874, 14–19.
23. Yang, D., Mosadegh, B., Ainla, A., Lee, B., Khashai, F., Suo, Z., Bertoldi, K., & Whitesides, G. M. (2015). Buckling of elastomeric beams enables actuation of soft machines. *Advanced Materials*, 27, 6323–6327.
24. Connolly, F., Polygerinos, P., Walsh, C. J., & Bertoldi, K. (2015). Mechanical programming of soft actuators by varying fiber angle. *Soft Robotics*, 2, 24–32.
25. Xiao, W., Du, X., Chen, W., Yang, G., Hu, D., & Han, X. (2021). Cooperative collapse of helical structure enables the actuation of twisting pneumatic artificial muscle. *International Journal of Mechanical Sciences*, 201, 106483.
26. Kim, S., Laschi, C., & Trimmer, B. (2013). Soft robotics: a new perspective in robot evolution. *Trends in Biotechnology*, 31, 287–294.
27. Mirvakili, S. M., & Hunter, I. W. (2018). Artificial muscles: mechanisms, applications, and challenges. *Advanced Materials*, 30, 1704407.
28. Hao, Y., Wang, T. M., Ren, Z. Y., Gong, Z. Y., Wang, H., Yang, X. B., Guan, S. Y., & Wen, L. (2017). Modeling and experiments of a soft robotic gripper in amphibious environments. *International Journal of Advanced Robotic Systems*, 14, 256010278.
29. Polygerinos, P., Wang, Z., Overvelde, J. T. B., Galloway, K. C., Wood, R. J., Bertoldi, K., & Walsh, C. J. (2015). Modeling of soft fiber-reinforced bending actuators. *Ieee Transactions on Robotics*, 31, 778–789.
30. Chen, W. B., Xiong, C. H., Liu, C. L., Li, P. M., & Chen, Y. H. (2019). Fabrication and dynamic modeling of bidirectional bending soft actuator integrated with optical waveguide curvature sensor. *Soft Robotics*, 6, 495–506.
31. Peele, B. N., Wallin, T. J., Zhao, H., & Shepherd, R. F. (2015). 3d printing antagonistic systems of artificial muscle using projection stereolithography. *Bioinspiration & Biomimetics*, 10, 55003.
32. Zhang, B. Y., Hu, C. Q., Yang, P. H., Liao, Z. X., & Liao, H. E. (2019). Design and modularization of multi-dof soft robotic actuators. *Ieee Robotics and Automation Letters*, 4, 2645–2652.
33. Sun, Y., Song, S., Liang, X., & Ren, H. (2016). A miniature soft robotic manipulator based on novel fabrication methods. *Ieee Robotics and Automation Letters*, 1, 617–623.
34. Elsayed, Y., Vincensi, A., Lekakou, C., Geng, T., Saaj, C. M., Ranzani, T., Cianchetti, M., & Menciassi, A. (2014). Finite element analysis and design optimization of a pneumatically actuating silicone module for robotic surgery applications. *Soft Robotics*, 1, 255–262.
35. Mao, Z., Nagaoka, T., Yokota, S., & Kim, J. (2020). Soft fiber-reinforced bending finger with three chambers actuated by ecf (electro-conjugate fluid) pumps. *Sensors and Actuators A: Physical*, 310, 112034.
36. Xiao, W., Hu, D., Chen, W. X., Yang, G., & Han, X. (2021). Modeling and analysis of bending pneumatic artificial muscle with multi-degree of freedom. *Smart Materials and Structures*, 30, 95018.
37. Mooney, M. (1940). A theory of large elastic deformation. *Journal of Applied Physics*, 11, 582–592.
38. Ogden, R. W. (1972). Large deformation isotropic elasticity—on the correlation of theory and experiment for incompressible rubberlike solids. *Proceedings of the Royal Society of London. A Mathematical and Physical Sciences*, 326, 565–584.
39. Yeoh, O. H. (1993). Some forms of the strain energy function for rubber. *Rubber Chemistry and Technology*, 66, 754–771.
40. Park, J. (1994). Optimal Latin-hypercube designs for computer experiments. *Journal of Statistical Planning and Inference*, 39, 95–111.
41. Gunst, R. F. (1996). Response surface methodology: process and product optimization using designed experiments. *Taylor & Francis*, 38, 284–286.
42. Hardy, R. L. (1971). Multiquadric equations of topography and other irregular surfaces. *Journal of geophysical research*, 76, 1905–1915.
43. Woodard, R. (2000). Interpolation of spatial data: some theory for kriging. *Technometrics*, 42, 436.
44. Yin, H. F., Wen, G. L., Liu, Z. B., & Qing, Q. X. (2014). Crash-worthiness optimization design for foam-filled multi-cell thin-walled structures. *Thin-Walled Structures*, 75, 8–17.
45. Coello, C. A. C., Pulido, G. T., & Lechuga, M. S. (2004). Handling multiple objectives with particle swarm optimization. *Ieee Transactions on Evolutionary Computation*, 8, 256–279.
46. Shintake, J., Cacucciolo, V., Floreano, D., & Shea, H. (2018). Soft robotic grippers. *Advanced Materials*, 30, 1707035.